

## Determination of transition dipole moments of solids with high-order harmonics driven by multicycle ultrashort pulses

Di Wu,<sup>1</sup> Liang Li,<sup>1,\*</sup> Yuntian Zhan,<sup>1</sup> Tengfei Huang,<sup>1</sup> Hubin Cui,<sup>1</sup> Jiapeng Li,<sup>1</sup> Pengfei Lan,<sup>1,†</sup> and Peixiang Lu<sup>1,2</sup>

<sup>1</sup>*Wuhan National Laboratory for Optoelectronics and School of Physics, Huazhong University of Science and Technology, Wuhan 430074, China*

<sup>2</sup>*Optical Valley Laboratory, Hubei 430074, China*



(Received 16 December 2021; accepted 13 May 2022; published 2 June 2022)

We propose an all-optical method to reconstruct the transition dipole moment of solid materials. Our method is realized by high-order harmonic generation driving by a multicycle laser pulse. The relations between the transition dipole moment and the harmonic yield are established. It is found that the transition dipole phase is related to the intensity ratio of the neighboring odd and even harmonics, and the modulus of the transition dipole moment is related to the odd harmonics. We investigate the high-order harmonic generation in symmetric crystals and asymmetric crystals by solving the semiconductor Bloch equations and use these relations to successfully reconstruct their relative transition dipole moments.

DOI: [10.1103/PhysRevA.105.063101](https://doi.org/10.1103/PhysRevA.105.063101)

### I. INTRODUCTION

The optical properties of solid materials are determined by the transition dipole moment (TDM), which describes the transition ability of electrons. The TDM texture reflects the nature of the electronic states, such as atomic orbital and interatomic bonding, and provides crucial insight into crystallographic structures, such as the band structure.

Accompanied by the rapid theoretical and experimental progress, many methods have been developed to measure the modulus and direction of TDM. The single-frequency hole burning spectrum [1] is used to measure the modulus of the TDM (mTDM). By using transient absorption spectroscopy with polarized probing in combination with different techniques such as Fourier-transform infrared spectroscopy [2] or fluorescence spectroscopy [3], one can obtain the orientation of the TDM in isotropic samples. However, it is difficult to determine the full orientation distribution function from measuring electronic transitions or the spatial orientations of fluorescence polarizing angles alone. Thus one uses magnetophotoselection effects [4] to obtain a precise determination of the 3D orientation of the TDM directly from isotropic samples. Using these methods, one can obtain the mTDM and the orientation of the TDM. However, there are few studies on measuring the distribution of TDM in the momentum space.

Recently, high-order harmonic generation (HHG) has been observed experimentally from a wide variety of solid media [5–10]. This suggests new approaches [11–19] for crystallographic analysis and probing the electronic properties of solids. By using HHG spectra driving by subcycle laser pulses [20], one can reconstruct the distribution of mTDMs in the momentum space. By using the interband resonance

high-order harmonic, one can reconstruct the structure of the two-dimensional TDM of black phosphorus at the isoenergy line in the momentum space [21]. However, the previous scheme requires sub-optical-cycle, carrier-envelope-phase-stable light pulses. It is challenging to accurately control and measure the carrier-envelope phase in experiments [22]. Moreover, the transition dipole phase (TDP) is not reconstructed, which plays an important role in solid HHG [23]. For asymmetric crystals, the TDP cannot be ignored and these schemes are no longer applicable.

In this work, we propose to use the HHG spectrum driving by multicycle laser pulses to reconstruct TDM. We theoretically establish the relationships between mTDM, TDP, and the harmonic yield. We numerically simulate HHG in symmetrical crystals and asymmetrical crystals, respectively, and successfully reconstruct their relative mTDMs and TDP by using these relationships. In addition, we verify the robustness of this scheme under various laser amplitudes.

This paper is organized as follows. In Sec. II A, we introduce the semiconductor Bloch equations for studying solid HHG. Then we establish the relationship between TDM and the harmonic yield in Sec. II B. The HHG process is numerically simulated. The results are shown in Sec. III. We reconstruct the TDMs of symmetric crystals (Sec. III A) and asymmetric crystals (Sec. III B), respectively. The summary is given in Sec. IV.

### II. THEORETICAL MODEL

#### A. Semiconductor Bloch equations

The HHG spectra can be obtained from the semiconductor Bloch equations (SBEs) [24–30], which have been proved to describe HHG well. We consider thin-layer materials that are not strongly correlated. When the degree of excitation is low, the electron-electron correlation [25,31–33] and the

\*liangl@hust.edu.cn

†pengfeilan@hust.edu.cn

propagation effects [34] can be neglected. Based on the single-active electron approximation and dipole approximation [26], the SBEs are given by (atomic units are used throughout this article unless stated otherwise)

$$\begin{aligned}\frac{d\pi(\mathbf{K}, t)}{dt} &= -\frac{\pi(\mathbf{K}, t)}{T_2} - i\xi(\mathbf{K}, t)[2N_v(\mathbf{K}, t) - 1]e^{-iS(\mathbf{K}, t)}, \\ \frac{dN_v(\mathbf{K}, t)}{dt} &= -i\xi^*(\mathbf{K}, t)\pi(\mathbf{K}, t)e^{iS(\mathbf{K}, t)} + \text{c.c.}, \\ \frac{d[N_v(\mathbf{K}, t) + N_c(\mathbf{K}, t)]}{dt} &= 0,\end{aligned}\quad (1)$$

where  $N_m$  ( $m = c, v$ ) is the band population.  $\pi(\mathbf{K}, t)$  is the off-diagonal element of the density matrix.  $\xi(\mathbf{K}, t) = \mathbf{F}(t) \cdot \mathbf{d}[\mathbf{K} + \mathbf{A}(t)]$  is the Rabi frequency and  $\mathbf{d}(\mathbf{k}) = \langle c, \mathbf{k} | \hat{\mathbf{r}} | v, \mathbf{k} \rangle$  represents the Bloch states.  $S(\mathbf{K}, t)$  is the classical action.  $\mathbf{K} = \mathbf{k} - \mathbf{A}(t)$  is the shifted crystal momentum and the vector potential  $\mathbf{A}(t)$  satisfies  $[d\mathbf{A}(t)/dt] = -\mathbf{F}(t)$ . The first Brillouin zone is also shifted to  $\overline{\mathbf{BZ}} = \mathbf{BZ} - \mathbf{A}(t)$ ;  $T_2$  is the dephasing time. We focus on the intensity of the primary plateau, which is not affected by the higher CB [20,35–37] when we consider wide separated bands crystals. Thus we use the two-band SBEs to calculate the harmonic spectrum of these crystals in this work.

The harmonic spectrum is obtained from the Fourier transform of the current. Their expressions are as follows:

$$\begin{aligned}\mathbf{J}_{ra}(t) &= \sum_{m=c,v} \int_{\overline{\mathbf{BZ}}} \mathbf{v}_m[\mathbf{k} + \mathbf{A}(t)] N_m(\mathbf{K}, t) d^3\mathbf{K}, \\ \mathbf{J}_{er}(t) &= \frac{d}{dt} \int_{\overline{\mathbf{BZ}}} \mathbf{d}[\mathbf{k} + \mathbf{A}(t)] \pi(\mathbf{K}, t) e^{iS(\mathbf{K}, t)} d^3\mathbf{K} + \text{c.c.},\end{aligned}\quad (2)$$

where  $\mathbf{v}_m(\mathbf{k}) = \nabla_{\mathbf{k}} E_m(\mathbf{k})$  is the group velocity in band  $m$  and  $E_m(\mathbf{k})$  is the band dispersion. The integration is carried out over the whole first Brillouin zone.

### B. Relationship between HHG and TDM

Note that the transition dipole moments are obtained based on the three-dimensional (3D) wave functions; we reduce the 3D problem to a 1D problem by projecting the 3D dipole moment onto the polarization direction of the driving laser. In this work, we consider a long-duration pulse. The ionization is dominant near the peak of the pulse and the effect of the pulse envelope can be ignored. With the parameters used in this work, the harmonics with the energies above the minimum band gap are dominated by the interband current, which has been also verified in recent research [20,26,28,38–41]. The generated high-order harmonic can be expressed by a series of emissions in time domain [42]

$$D(t) = \sum_{t', t_r, k_0}^{c,v} a_{cv}(t', t_r, k_0) e^{-iS_{cv}(t', t_r, k_0)} p_{cv}(t', t_r, k_0),$$

where  $D(t)$  is the interband current,  $k_0$  is the crystal momentum for the electron, and  $c, v$  are the band indexes.  $t'$  is the ionization moment,  $t_r$  is the recombination moment,  $a_{cv}(t', t_r, k_0)$  is the weight of the channel, and  $p_{cv}(t', t_r, k_0)$  is the polarization between the electron-hole pairs when recombination occurs. Note that  $p_{cv}(k) = -[E_c(k) - E_v(k)]d_{cv}(k)$  and

$a_{cv}(t', t_r, k_0) \propto d_{cv}(k') \cdot F(t')$ . Here  $S$  is the classical action,

$$\begin{aligned}S_{cv}(t', t_r, k_0) &= \int_{t'}^{t_r} \varepsilon_c^{k(\tau)} - \varepsilon_v^{k(\tau)} d\tau \\ &\quad - \int_Q [d_{cc}^k - d_{vv}^k] dk - [\theta_{cv}^{k(t_r)} - \theta_{cv}^{k(t')}],\end{aligned}\quad (3)$$

where  $\theta_{cv}^k$  is the phase of  $d(k)$ ;  $Q$  is the evolution path of  $k(t)$  from  $t'$  to  $t_r$ . This action includes the Berry connections and TDPs. It is proved to be gauge invariant [43,44].

The harmonic spectrum can be calculated by Fourier transformation of  $D(t)$ :

$$I(\omega) = \left| \int D(t) e^{-i\omega t} dt \right|^2.\quad (4)$$

In an optical cycle, there are two dominant emissions  $[D_1(t), D_2(t + T_0/2)]$ , which are contributed by the electrons ionized around the instantaneous maximum of the driving field. Notice that  $D_2(t + T_0/2) = D_1(t) e^{i(\pi + \Delta S)}$ . Here  $\Delta S = S_2 - S_1$  is the phase difference between the emissions 1 and 2 and  $\pi$  phase shift is due to the reversal sign of the electric field. The Fourier transform of these emissions are expressed as

$$\begin{aligned}D_1(\omega) &= \int D_1(t) e^{-i\omega t} dt \\ &\propto d^*(k_r) d(k') F(t') e^{-i\omega t - iS(t', t_r, k_r) - \frac{t_r - t'}{T_2}}, \\ D_2(\omega) &= \int D_2(t) e^{-i\omega t} dt = \int D_1\left(t - \frac{T_0}{2}\right) e^{i(\pi + \Delta S)} e^{-i\omega t} dt \\ &= D_1(\omega) e^{i(\pi + \Delta S - \omega \frac{T_0}{2})},\end{aligned}\quad (5)$$

where  $F$  is the laser electric field,  $\omega = N\omega_0$ ,  $\omega_0$  is the frequency of the laser pulse, and  $N$  is the harmonic order. Therefore, the yield of the  $N$ th harmonic can be given by

$$\begin{aligned}I_N &= |D_1(\omega) + D_2(\omega)|^2 \\ &\propto \left| d^*(k_r) d(k') F(t') e^{\frac{t_r - t'}{T_2}} (1 - e^{i(\Delta S - N\pi)}) \right|^2.\end{aligned}\quad (6)$$

For the symmetric crystals, the Berry connections are zero and TDP is constant [43]. The action is  $S(t', t_r, k_r) = \int_{t'}^{t_r} \varepsilon_c^{k(\tau)} - \varepsilon_v^{k(\tau)} d\tau = S(t' + \frac{T_0}{2}, t_r + \frac{T_0}{2}, -k_r)$  and  $\Delta S = 0$ . Therefore, the yield of the  $N$ th harmonic is as follows:

$$I_N \propto \left| d^*(k_r) d(k') F(t') e^{\frac{t_r - t'}{T_2}} (1 - e^{-iN\pi}) \right|^2.\quad (7)$$

Clearly  $I_N = 0$  for even harmonics; the harmonic spectrum consists of odd harmonics only. Then we take the ratio of the neighboring odd harmonics ( $I_{2n-1}, I_{2n+1}$ ),

$$\begin{aligned}\frac{I_{2n-1}}{I_{2n+1}} &= \left| \frac{d^*(k_r^{2n-1}) d(k'^{2n-1}) F(t'^{2n-1}) e^{\frac{t_r^{2n-1} - t'^{2n-1}}{T_2}}}{d^*(k_r^{2n+1}) d(k'^{2n+1}) F(t'^{2n+1}) e^{\frac{t_r^{2n+1} - t'^{2n+1}}{T_2}}} \right|^2 \\ &= \left| \frac{d(k_r^{2n-1})}{d(k_r^{2n+1})} \right|^2,\end{aligned}\quad (8)$$

where the  $k_r^N$  is the lattice momentum  $k_r$  corresponding to the  $N$ th harmonic. In this work, we consider the direct band-gap

crystals where the minimum band gap is at the high-symmetry  $\Gamma$  point of the Brillouin zone. Driven by linearly polarized long-duration pulses, the electrons ionized near the  $\Gamma$  point contribute predominantly to the HHG because the harmonics generated by them are constructive interference [42]. The TDM  $d(k')$  at ionization times are approximately equal to TDM at the  $\Gamma$  point. Note that the ionization is dominant near the peak of the pulse. The field strengths  $F(t')$  in the neighboring high-order harmonics are approximately equal. Moreover, for the neighboring high-order harmonics, the electron acceleration time  $t_r - t'$  is approximately equal [18,20]. Thus the dephase time terms  $e^{-\frac{t_r - t'}{T_2}}$  are approximately equal. Our reconstruction applies to the case where the excitation happens at the localized  $\Gamma$  point at the moment near the peak of the electric field. Within these conditions, we can get Eq. (8) to reconstruct TDM. Then we can map the reconstruction result to the momentum space according to the law of conservation of energy.

For the asymmetric systems, since the Berry connection and the TDP are not zero, the action  $S(t', t_r, k_r)$  separated by  $T_0/2$  is not equal. We set  $\Delta\Theta = \int_Q (d_{cc}^k - d_{vv}^k) dk + \theta_{cv}^{k(t')} - \theta_{cv}^{k(t)}$ , which is a gauge-invariant quantity [43–45]. The expressions of action  $S(t', t_r, k_r)$  become

$$S(t', t_r, k_r) = \int_{t'_s}^{t_s} \varepsilon_c^{k(\tau)} - \varepsilon_v^{k(\tau)} d\tau - \Delta\Theta,$$

$$S\left(t' + \frac{T_0}{2}, t_r + \frac{T_0}{2}, -k_r\right) = \int_{t'_s + \frac{T_0}{2}}^{t_s + \frac{T_0}{2}} \varepsilon_c^{k(\tau)} - \varepsilon_v^{k(\tau)} d\tau + \Delta\Theta,$$

$$\Delta S = 2\Delta\Theta. \quad (9)$$

It is shown that there is always a set of basis functions  $\varphi_n(k)$  leading to  $\partial_k \varphi_n(k) = d_{mn}^k = 0$  [43,46]. Now  $\Delta\Theta = \Delta\theta = \theta(k') - \theta(k_r)$ ; then we substitute them into Eq. (6),

$$I_N \propto \left| d^*(k_r) d(k') F(t') e^{\frac{t_r - t'}{T_2}} (e^{-i\Delta\theta} - e^{i\Delta\theta} e^{-iN\pi}) \right|^2. \quad (10)$$

We can get the yield of odd harmonics and even harmonics,

$$I_{2n} \propto |d^*(k_r^{2n}) d(k_r^{2n}) \sin(\Delta\theta)|^2,$$

$$I_{2n+1} \propto |d^*(k_r^{2n+1}) d(k_r^{2n+1}) \cos(\Delta\theta)|^2. \quad (11)$$

Considering that the absolute value of the TDM changes smoothly with momentum, the factor  $|d^*(k_r)|$  is approximately equal for the neighboring high-order harmonics. Moreover, because the electrons are mainly excited from the  $\Gamma$  point, the TDP at  $\Gamma$  point  $\theta(k')$  is set to zero. The intensity ratio of the neighboring odd and even harmonics is given by

$$\frac{I_{2n}}{I_{2n+1}} = \tan^2 \theta(k_r^{2n+1}). \quad (12)$$

Then by substituting Eq. (12) into Eq. (8), we can get the relationship between mTDM and the harmonic yield,

$$\frac{I_{2n-1}}{I_{2n+1}} = \left| \frac{d(k_r^{2n-1}) \cos[\theta(k_r^{2n-1})]}{d(k_r^{2n+1}) \cos[\theta(k_r^{2n+1})]} \right|^2. \quad (13)$$

The TDP and the relative values of mTDM can be reconstructed by using Eq. (13) and Eq. (12). Our scheme combines

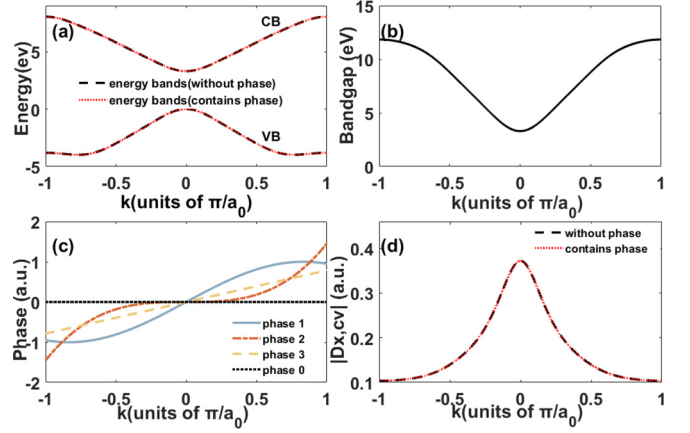


FIG. 1. (a) Energy bands of symmetrical (black dashed line) and asymmetrical crystals (red dotted line). The valence ( $m = v$ ) and conduction ( $m = c$ ) band come from the energy bands in the  $X - \Gamma$  direction of ZnO. (b) The band gap of these materials. (c) The TDPs of symmetrical crystal (phase 0) and asymmetric crystal (phases 1,2,3). (d) The mTDMs of symmetrical crystal (black dashed line) and asymmetric crystal (red dotted line).

the experiment [1] that measures the average TDM size; the magnitude of TDM can be determined.

### III. RESULTS AND DISCUSSION

Similar to Refs. [12,13,35,37], we consider the HHG from crystal with wide separated bands, where only two bands, i.e., one CB and one VB, are dominant in the HHG process. Figure 1(a) shows the energy bands of symmetric crystals (black dashed line) and asymmetric crystals (red dotted line), in which the two bands are marked by VB and CB. Figure 1(b) shows their band gaps, in which the minimum band-gap energy between CB and VB is  $E_g = 0.1213$  a.u. (3.3 eV). The mTDMs and TDPs are shown in Figs. 1(d) and 1(c), respectively. The TDP of symmetric crystals (phase 0) is zero for all crystal momentum due to the inversion symmetry. In contrast, there exists nonzero TDPs for asymmetric crystals (phase 1,2,3). To demonstrate our scheme, we set the TDPs as  $\sin(a_0 k_x) \frac{\pi}{4}$  (phase 1),  $(\frac{1}{4} a_0 k_x)^3$  (phase 2), and  $\frac{1}{4} a_0 k_x$  (phase 3). At the same time, the mTDMs of these crystals are set to the same.

#### A. Symmetric crystal

We first demonstrate our scheme in a symmetrical crystal [phase 0 in Fig. 1(c)]. We use the finite difference method to solve the time evolution process. The  $k_x$  axis in reciprocal space is discretized by 481 points. The step size of the time grid is 0.537 a.u. The wavelength and intensity of the laser pulses are  $3.9 \mu\text{m}$  ( $\omega_0 = 0.0117$  a.u.) and  $7.2 \times 10^{11} \text{ W/cm}^2$  ( $F_0 = 0.004$  a.u.). The electric-field waveform is a trapezoidal envelope of  $30T_0$ , where  $T_0 = (2\pi/\omega_0)$  is an optical cycle.  $T_2$  is the dephasing time, which is set to 1.2 fs [47,48] in this work.

Figure 2(a) shows the solid harmonic spectrum generated from multicycle laser pulses. The red line in this figure marks the minimum band gap. We can see that the harmonic

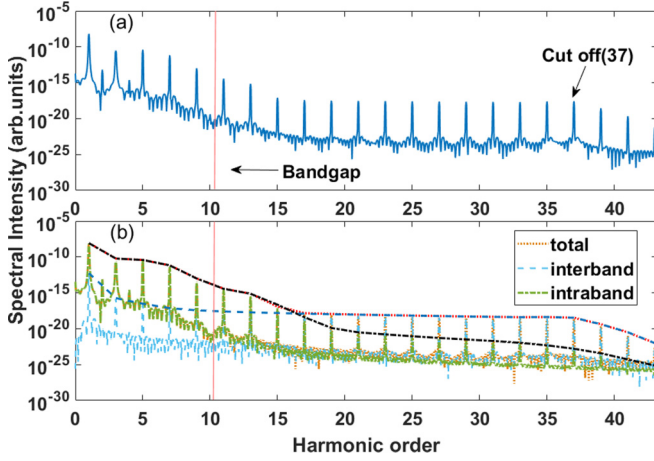


FIG. 2. (a) Total HHG spectrum of the symmetric crystal (blue solid curve). (b) The HHG spectrum produced by interband (light blue dashed curve) and intraband currents (green dash-dotted curve). The orange dotted curve is the total HHG spectrum. The red dotted curve is the total harmonic peak variation curve and the blue dashed (black dash-dotted) curve is the interband (intraband) harmonic peak variation curve.

spectrum consists of odd harmonics only. The HHG spectrum has a falloff, of eight or nine orders of magnitude, from the 3rd to the 17th harmonic. Then a plateau appears for the 17th to 37th harmonics, where the harmonic intensities remain approximately constant. Finally, the harmonics spectrum drops rapidly near the 37th harmonic. To compare the contributions of the intraband current and the interband polarization to the total harmonic spectrum, we show their harmonic spectrum in Fig. 2(b). Below the 15th harmonics, the intraband harmonics (the black dash-dotted line) are three to five orders of magnitude higher than the interband harmonics (the blue dashed line). In the 15th to 17th harmonics, the two contributions become comparable with intraband HHG being slightly stronger. Above the 17th harmonics, the intensity of the interband harmonic spectrum is two to four orders of magnitude higher than that of the intraband. Thus the interband current dominates the intraband contribution in the plateau. We choose the harmonics in the plateau region to reconstruct TDM.

After obtaining the harmonic spectrum, the relative value of the TDM can be calculated by Eq. (8). To get the distribution of TDM in the momentum space, we found the mapping relationship between the harmonic order and the lattice momentum (black solid line) through the dispersion relationship, as presented in Fig. 3(a). It can be seen that the lattice momentum corresponding to these points (the abscissa of the red solid point) can reach near the boundary of the Brillouin zone. Figure 3(b) shows the distribution of reconstructed TDM in the momentum space. Since Eq. (8) calculates the relative value of TDM, we normalize the target TDM in the same order. The target TDM is a slowly descending curve (blue dash-dotted curve) and the solid pink points are the reconstructed TDM. By comparing the target TDM with the reconstructed TDM, it can be observed that the mapped  $k$ -dependent TDM in most points is closely consistent with the target TDM.

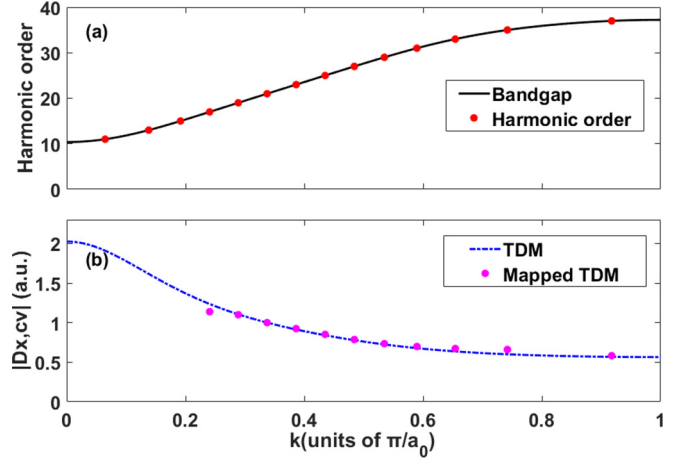


FIG. 3. (a) Mapping relationship between the harmonic order and the lattice momentum. The red solid points are the sampling points and the black solid line is derived from band gap. (b) For comparison, the target TDM (blue dash-dotted line) and the reconstruction of the TDM (pink solid point) by using the total HHG spectrum of Fig. 2 are presented here.

## B. Asymmetric crystal

Next, we discuss the reconstruction in asymmetric crystals, in which their TDPs correspond to phases 1, 2, and 3 in Fig. 1(c). The laser parameters are the same with Sec. III A. Their total harmonic spectra are shown in Fig. 4. The blue, red, and black lines correspond to the harmonic spectra of phase 1, 2, and 3, respectively. These harmonic spectra still have a rapid decline below the 17th order, and then form a plateau in the 17th to 37th order, and cut off above the 37th order. In addition, even harmonics appear in these harmonic spectra.

According to Eq. (13) and Eq. (12), the TDP and the mTDM corresponding to each order can be calculated. Same as Fig. 3, we can get the distribution of reconstruction results in the momentum space. Figure 5(b) shows the reconstruction results of our three forms of TDP. The solid line is the target TDP and the points (black circle, pink square, and green diamond) are the reconstructed TDPs. We can see that whether

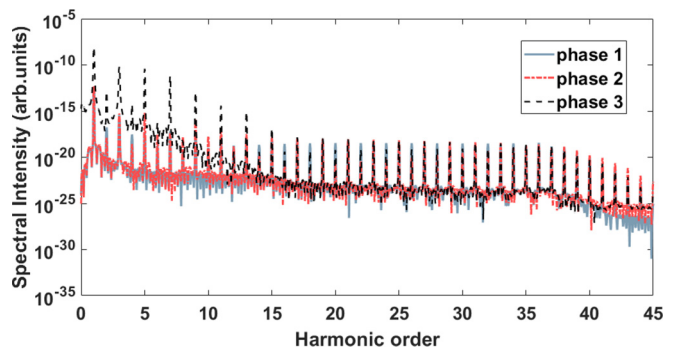


FIG. 4. Total harmonic spectrum from the two-band calculation when TDP is phase 1,2,3, respectively. The laser parameters are 3900 nm in wavelength,  $7.2 \times 10^{11}$  W/cm<sup>2</sup> in intensity, and the waveform of the electric field is a trapezoidal envelope of 30 optical cycles.

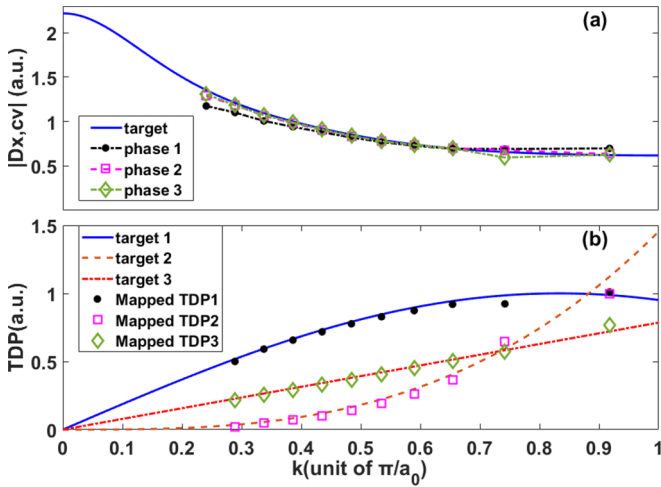


FIG. 5. (a) Target TDM (blue solid line) and the reconstructed mTDMs under different TDPs (black circle, pink square, and green diamond). (b) The target TDPs (blue solid line, orange dashed line, and red dash-dotted line) and the reconstructed TDPs (black circle, pink square, and green diamond).

it is a saturated, linear, or cubic TDP, the reconstruction results are in good agreement with the target TDP. In Fig. 5(a), the solid line is the target mTDM and the dashed lines are the reconstruction results. In these three cases, the mapped mTDMs (black circle, pink square, and green diamond) in most points is consistent with the target mTDM (blue solid line).

To examine the robustness of our scheme under the laser amplitude, we reconstruct the TDM under various field strengths. Through numerical simulation, the field strength range in this work is 0.0038 a.u. to 0.0052 a.u. We choose phase 3 and keep other parameters (except electric-field strength) consistent with Sec. III A. Figures 6(a) and 6(b) respectively show the reconstructed mTDMs and TDPs. It can be seen that most reconstruction points do not change much with intensity and they are all near the target curve except for the points near the boundary of the Brillouin zone. The harmonics corresponding to the points on the boundary of the Brillouin zone are close to the cutoff and are sensitive to changes in electric-field strength, resulting in some small changes in the reconstruction results. Therefore, our scheme can accurately reconstruct TDM in a large field strength range.

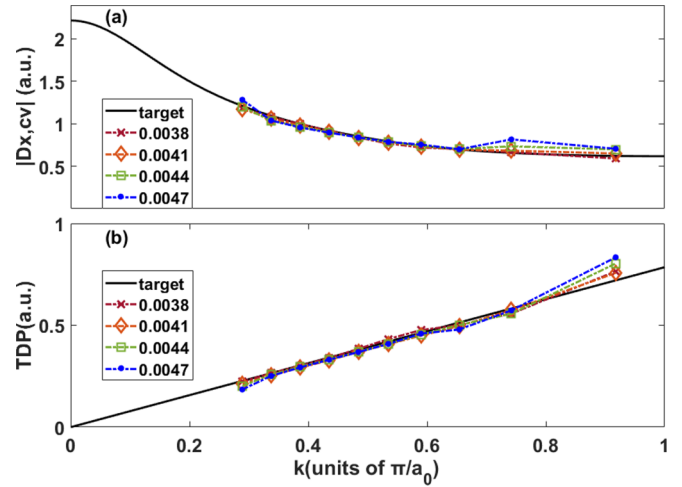


FIG. 6. Reconstruction results under various field strengths. (a) The target mTDM (black solid line) and the reconstructed mTDMs under different field strengths (dark red cross, orange diamond, green square, and blue solid circle). (b) The target TDP (black solid line) and the reconstructed TDPs under different field strengths (dash-dotted lines with different data point symbols).

#### IV. SUMMARY

In this work, we successfully reconstruct the relative distribution of mTDM and TDP in one-dimensional momentum space. In our scheme, the reconstruction is based on the relation between the mTDM, TDP, and the intensity of harmonics in the plateau region, in which solid high-order harmonics are driven by multicycle laser pulses. Our scheme applies to both symmetric crystals and asymmetric crystals and can accurately reconstruct the relative mTDM and TDP in a large field strength range. The success of the all-optical method would pave the way for exploring the distribution of TDM in two-dimensional momentum space.

#### ACKNOWLEDGMENT

This work was supported by National Natural Science Foundation of China (Grants No. 11874165, No. 91950202, No. 11627809, No. 11934006, No. 12021004, and No. 12104172).

- [1] B. Lauritzen, N. Timoney, N. Gisin, M. Afzelius, H. de Riedmatten, Y. Sun, R. M. Macfarlane, and R. L. Cone, *Phys. Rev. B* **85**, 115111 (2012).
- [2] M. Theisen, M. Linke, M. Kerbs, H. Fidder, M. E. A. Madjet, A. Zacarias, and K. Heyne, *J. Chem. Phys.* **131**, 124511 (2009).
- [3] T. Mu, S. Chen, Y. Zhang, P. Guo, and H. Chen, *Opt. Express* **23**, 11748 (2015).
- [4] A. Toffoletti, Z. J. Wang, J. Z. Zhao, M. Tommasini, and A. Barbon, *Phys. Chem. Chem. Phys.* **20**, 20497 (2018).
- [5] S. Ghimire, A. D. DiChiara, E. Sistrunk, P. Agostini, L. F. DiMauro, and D. A. Reis, *Nat. Phys.* **7**, 138 (2011).
- [6] N. Yoshikawa, T. Tamaya, and K. Tanaka, *Science* **356**, 736 (2017).
- [7] O. Schubert, M. Hohenleutner, F. Langer, B. Urbanek, C. Lange, U. Huttner, D. Golde, T. Meier, M. Kira, S. W. Koch, and R. Huber, *Nat. Photon.* **8**, 119 (2014).
- [8] Y. S. You, D. A. Reis, and S. Ghimire, *Nat. Phys.* **13**, 345 (2017).
- [9] T. T. Luu, M. Garg, S. Y. Kruchinin, A. Moulet, M. T. Hassan, and E. Goulielmakis, *Nature (London)* **521**, 498 (2015).
- [10] H. Liu, Y. Li, Y. S. You, S. Ghimire, T. F. Heinz, and D. A. Reis, *Nat. Phys.* **13**, 262 (2017).

- [11] C. Yu, S. Jiang, T. Wu, G. Yuan, Z. Wang, C. Jin, and R. Lu, *Phys. Rev. B* **98**, 085439 (2018).
- [12] G. Vampa, T. J. Hammond, N. Thiré, B. E. Schmidt, F. Légaré, C. R. McDonald, T. Brabec, D. D. Klug, and P. B. Corkum, *Phys. Rev. Lett.* **115**, 193603 (2015).
- [13] A. A. Lanin, E. A. Stepanov, A. B. Fedotov, and A. M. Zheltikov, *Optica* **4**, 516 (2017).
- [14] F. Yang, X. D. Xu, and R. B. Liu, *New J. Phys.* **16**, 043014 (2014).
- [15] T. T. Luu and H. J. Wörner, *Nat. Commun.* **9**, 916 (2018).
- [16] D. Bauer and K. K. Hansen, *Phys. Rev. Lett.* **120**, 177401 (2018).
- [17] A. Chacón, D. Kim, W. Zhu, S. P. Kelly, A. Dauphin, E. Pisanty, A. S. Maxwell, A. Picón, M. F. Ciappina, D. E. Kim, C. Ticknor, A. Saxena, and M. Lewenstein, *Phys. Rev. B* **102**, 134115 (2020).
- [18] L. Li, P. F. Lan, L. X. He, W. Cao, Q. B. Zhang, and P. X. Lu, *Phys. Rev. Lett.* **124**, 157403 (2020).
- [19] M. K. Hagen and S. W. Koch, *Phys. Status Solidi RRL* **15**, 2100397 (2021).
- [20] Y. T. Zhao, S. Y. Ma, S. C. Jiang, Y. J. Yang, X. Zhao, and J. G. Chen, *Opt. Express* **27**, 34393 (2019).
- [21] K. Uchida, V. Pareek, K. Nagai, K. M. Dani, and K. Tanaka, *Phys. Rev. B* **103**, L161406 (2021).
- [22] C. Manzoni, O. D. Mücke, G. Cirmi, S. B. Fang, J. Moses, S. W. Huang, K. H. Hong, G. Cerullo, and F. X. Kartner, *Laser Photon. Rev.* **9**, 129 (2015).
- [23] S. C. Jiang, H. Wei, J. G. Chen, C. Yu, R. F. Lu, and C. D. Lin, *Phys. Rev. A* **96**, 053850 (2017).
- [24] M. Garg, M. Zhan, T. T. Luu, H. Lakhotia, T. Klostermann, A. Guggenmos, and E. Goulielmakis, *Nature (London)* **538**, 359 (2016).
- [25] D. Golde, T. Meier, and S. W. Koch, *Phys. Rev. B* **77**, 075330 (2008).
- [26] G. Vampa, C. R. McDonald, G. Orlando, D. D. Klug, P. B. Corkum, and T. Brabec, *Phys. Rev. Lett.* **113**, 073901 (2014).
- [27] C. Yu, S. C. Jiang, and R. F. Lu, *Adv. Phys.-X* **4**, 1562982 (2019).
- [28] G. Vampa, C. R. McDonald, G. Orlando, P. B. Corkum, and T. Brabec, *Phys. Rev. B* **91**, 064302 (2015).
- [29] G. Vampa, T. J. Hammond, N. Thire, B. E. Schmidt, F. Legare, C. R. McDonald, T. Brabec, and P. B. Corkum, *Nature (London)* **542**, 260 (2017).
- [30] J. Li, S. Fu, H. Wang, X. Zhang, B. Ding, B. Hu, and H. Du, *Phys. Rev. A* **98**, 043409 (2018).
- [31] K. K. Hansen, T. Deffge, and D. Bauer, *Phys. Rev. A* **96**, 053418 (2017).
- [32] S. V. B. Jensen and L. B. Madsen, *Phys. Rev. B* **104**, 054309 (2021).
- [33] J.-Q. Liu and X.-B. Bian, *Phys. Rev. B* **102**, 174302 (2020).
- [34] P. Xia, C. Kim, F. Lu, T. Kanai, H. Akiyama, J. Itatani, and N. Ishii, *Opt. Express* **26**, 29393 (2018).
- [35] M. Wu, S. Ghimire, D. A. Reis, K. J. Schafer, and M. B. Gaarde, *Phys. Rev. A* **91**, 043839 (2015).
- [36] Y. T. Zhao, S. C. Jiang, X. Zhao, J. G. Chen, and Y. J. Yang, *Opt. Lett.* **45**, 2874 (2020).
- [37] C. R. McDonald, G. Vampa, P. B. Corkum, and T. Brabec, *Phys. Rev. A* **92**, 033845 (2015).
- [38] Y. S. You, M. Wu, Y. Yin, A. Chew, X. Ren, S. Gholam-Mirzaei, D. A. Browne, M. Chini, Z. Chang, K. J. Schafer, M. B. Gaarde, and S. Ghimire, *Opt. Lett.* **42**, 1816 (2017).
- [39] M. Wu, D. A. Browne, K. J. Schafer, and M. B. Gaarde, *Phys. Rev. A* **94**, 063403 (2016).
- [40] N. Yoshikawa, K. Nagai, K. Uchida, Y. Takaguchi, S. Sasaki, Y. Miyata, and K. Tanaka, *Nat. Commun.* **10**, 3709 (2019).
- [41] A. J. Uzan, G. Orenstein, A. Jimenez-Galan, C. McDonald, R. E. F. Silva, B. D. Bruner, N. D. Klimkin, V. Blanchet, T. Arusi-Parpar, M. Kruger, A. N. Rubtsov, O. Smirnova, M. Ivanov, B. H. Yan, T. Brabec, and N. Dudovich, *Nat. Photon.* **14**, 183 (2020).
- [42] L. Li, P. F. Lan, X. S. Zhu, T. F. Huang, Q. B. Zhang, M. Lein, and P. X. Lu, *Phys. Rev. Lett.* **122**, 193901 (2019).
- [43] J. B. Li, X. Zhang, S. L. Fu, Y. K. Feng, B. T. Hu, and H. C. Du, *Phys. Rev. A* **100**, 043404 (2019).
- [44] L. Yue and M. B. Gaarde, *Phys. Rev. A* **101**, 053411 (2020).
- [45] S. C. Jiang, C. Yu, J. G. Chen, Y. W. Huang, R. F. Lu, and C. D. Lin, *Phys. Rev. B* **102**, 155201 (2020).
- [46] U. Lindelfelt, H. E. Nilsson, and M. Hjelm, *Semicond. Sci. Technol.* **19**, 1061 (2004).
- [47] M. Hohenleutner, F. Langer, O. Schubert, M. Knorr, U. Huttner, S. W. Koch, M. Kira, and R. Huber, *Nature (London)* **523**, 572 (2015).
- [48] T. T. Luu and H. J. Wörner, *Phys. Rev. B* **94**, 115164 (2016).